

財團法人國防工業發展基金會 便簽

核判 權責
董事長
執行長
V
秘書

- 一、 國立臺灣大學工學院材料科學與工程學系研究所(以下簡稱材料所)陳天玥博士生畢業論文公告案。
- 二、 國立臺灣大學材料所陳天玥博士生原支領本會 109 年度國防工業獎學金，渠於今(110)年 10 月 13 日畢業離校(如附呈 1)，畢業後繼續於材料所實驗室從事博士後研究，尚未正式就業。
- 三、 陳博士畢業論文題目「調控過渡金屬/鐵磁異質結構之自旋軌道矩效率」(英文版)，按本會「國防工業獎學金發放作業規定」第五點獎學金受領人義務(三)規定，提供畢業論文 2 本及電子檔，並於論文致謝誌中表達對本會之感謝。另按同規定第七點成果運用，畢業論文無償提供本會或本會指定之公法人、政府機關(構)運用。(如附呈 2)
- 四、 陳博士畢業論文主頁及中、英文摘要、目錄等擬於本會網站公告(如附件)，提供國防部研究單位(如：國防部軍備局、中科院、國防安全研究院、軍事院校等)有需求可洽本會索取。
- 五、 請核示。

承辦單位：

會計員葉恒菁
11010190900

督導管理歐仲偉
11010190930

秘書謝日升
11010191110



國立臺灣大學工學院材料科學與工程學系暨研究所

博士論文

Department of Materials Science and Engineering

College of Engineering

National Taiwan University

Doctoral Dissertation



調控過渡金屬/鐵磁異質結構之自旋軌道矩效率

Engineering of spin-orbit torque efficiency in transition
metal/ferromagnet magnetic heterostructures

陳天玥

Tian-Yue Chen

指導教授：白奇峰 博士

Advisor: Chi-Feng Pai, Ph.D.

中華民國 110 年 9 月

September, 2021

國立臺灣大學博士學位論文

口試委員會審定書

論文中文題目： 調控過渡金屬/鐵磁異質結構之自旋軌道矩
效率

論文英文題目： Engineering of spin-orbit torque efficiency
in transition metal/ferromagnet magnetic
heterostructures

本論文係陳天玥君（F05527067）在國立臺灣大學材料
科學與工程學系、所完成之博士學位論文，於民國 110 年 09
月 14 日承下列考試委員審查通過及口試及格，特此證明

口試委員：白奇峰 白奇峰
(指導教授)

郭光宇 郭光宇

林昭吟 林昭吟

黃斯衍 黃斯衍

曲丹茹 曲丹茹

系主任、所長 謝宗霖 謝宗霖 (簽名)

致謝

在就讀研究所的這段時間，一路上都受到很多的幫助，才能支持我完成這份研究論文和博士學位。

首先，我想特別感謝指導教授，白奇峰教授。在學習之初，儘管對於這個領域完全不了解，老師還是保持耐心並時常親自指導，讓我一步一步對自旋電子學有更深的認識。也是因為老師對實驗的熱情，感染我在這個領域繼續學習。感謝老師的信任，給我很大的自由度，讓我在不同階段完成不一樣的目標。

感謝黃斯衍教授和黃老師實驗室的莊造奇學姊、梁夏菱同學。感謝黃老師在實驗室草創之初，願意讓我學習及使用相關的儀器。和黃老師一起參加各項會議時，受到很多的照顧，也獲益良多。謝謝莊造奇學姊，很認真的教導我各項儀器的使用，也為我耐心解答了很多關於這個領域的疑問。除了專業知識外，她也時常分享許多經驗，讓我度過遇到的關卡。也謝謝梁夏菱同學在實驗上的幫助，如果沒有她們一直以來的幫助，很多實驗都無法順利地完成。

特別感謝蔡宗佑同學，從剛進實驗室一直到现在就受到他很多的照顧，也因為認識他，所以接觸了許多不同的人事物。和他一起做實驗的那段時間，也是在研究所生涯中最享受的一段日子。雖然他時常用尖銳的言語激勵我，但是在相互討論的過程中，可以看見自己不足的地方，也總能學習到很多不同的知識。同時，也感謝廖唯邦同學、彭成瑋同學，在這段時間也合作完成了 many 許多實驗。

非常感謝所有幫助過我和在這段旅程中認識的人，中研院李尚凡老師實驗室的蔡禮在學長，謝謝你在光學實驗上的經驗分享；清大郭瑞年老師實驗室的劉有麒學長，在合作的過程中讓我更了解不一樣領域的知識；在美國讀書的許有恆學長，謝謝你在 2017 MMM 的時候主動和我交談，在人生地不熟的地方感受到最溫暖的關心，也開啟了後續許多的交流。也特別感謝實驗室的蕭佑展同學，看到你對實驗慢慢產生興趣，是最感動的事情之一。這不只是你自己的成長，也是對我最大的肯定。謝謝 Neil，我們一起解決了許多儀器的問題，你讓實驗室變得

有趣許多。也感謝一起來台北念書的朋友們。剛來台北生活，時常在課餘時一起探索台北這個城市的美好。這段回憶一直到現在都是心中很珍貴的一部分，也因為有他們的陪伴，讓我度過在課業及生活上極大的不適應。

最後感謝我的家人，謝謝你們支持我繼續攻讀博士班，讓我也能夠放心的完成學業。謝謝所有在這段旅程中幫助過我的人，也因為你們的陪伴，我才能完成這份論文。

本論文獲財團法人國防工業發展基金會獎學金贊助。

LIST OF PUBLICATIONS

- [1] Ting-Yu Chang, Chih-Lin Cheng, Chao-Chung Huang, Cheng-Wei Peng, Yu-Hao Huang, Tian-Yue Chen, Yan-Ting Liu, and Chi-Feng Pai*, “*Large unidirectional magnetoresistance in metallic heterostructures in the spin transfer torque regime*”, Physical Review B, 104 (2), 024432 (2021)
- [2] Cheng-Wei Peng, Wei-Bang Liao, Tian-Yue Chen, and Chi-Feng Pai*, ”*Efficient spin-orbit torque generation in semiconducting WTe₂ with hopping transport*”, ACS Applied Materials & Interfaces 13 (13), 15950-15957 (2021)
- [3] Wei-Bang Liao, Tian-Yue Chen, Yu-Chan Hsiao, and Chi-Feng Pai*, “*Pulse-width and temperature dependence of memristive spin-orbit torque switching*” Applied Physics Letters 117 (18), 182402 (2020)
- [4] Yan-Ting Liu, Tian-Yue Chen[†], Tze-Hsiang Lo, Tsung-Yu Tsai, Shan-Yi Yang, Yao-Jen Chang, Jeng-Hua Wei, and Chi-Feng Pai*, “*Determination of spin-orbit-torque efficiencies in heterostructures with in-plane magnetic anisotropy*” Physical Review Applied 13 (4), 044032 (2020)
- [5] Tsung-Yi Chen, Wei-Bang Liao, Tian-Yue Chen, Tsung-Yu Tsai, Cheng-Wei Peng, and Chi-Feng Pai*, “*Current-induced spin-orbit torque efficiencies in W/Pt/Co/Pt heterostructures*” Applied Physics Letters 116 (7), 072405 (2020)
- [6] Tian-Yue Chen, Cheng-Wei Peng, Tsung-Yu Tsai, Wei-Bang Liao, Chun-Te Wu, Hung-Wei Yen, and Chi-Feng Pai*, “*Efficient spin-orbit torque switching with nonepitaxial chalcogenide heterostructures*” ACS applied materials & interfaces 12 (6), 7788-7794 (2020)
- [7] Wei-Bang Liao, Tian-Yue Chen, Yari Ferrante, Stuart Parkin, and Chi-Feng Pai*, “*Current-induced magnetization switching by the high spin Hall conductivity a-W*” physica status solidi (RRL)–Rapid Research Letters 13 (11), 190040 (2019)

- [8] Tian-Yue Chen, YongXi Ou, Tsung-Yu Tsai, Robert A. Buhrman, and Chi-Feng Pai*, “*Spin-orbit torques acting upon a perpendicularly magnetized Py layer*” APL Materials 6 (12), 121101 (2018)
- [9] Tian-Yue Chen, Hsin-I Chan, Wei-Bang Liao, and Chi-Feng Pai*, “*Current-induced spin-orbit torque and field-free switching in Mo-based magnetic heterostructures*” Physical Review Applied 10 (4), 044038 (2018)
- [10] Tsung-Yu Tsai, Tian-Yue Chen, Chun-Ting Wu, Hsin-I Chan, and Chi-Feng Pai*, “*Spin-orbit torque magnetometry by wide-field magneto-optical Kerr effect*” Scientific reports 8 (1), 1-8 (2018)
- [11] Ting-Chien Wang, Tian-Yue Chen^t, Chun-Te Wu, Hung-Wei Yen, and Chi-Feng Pai*, “*Comparative study on spin-orbit torque efficiencies from W/ferromagnetic and W/ferrimagnetic heterostructures*” Physical Review Materials 2 (1), 014403 (2018)
- [12] Tian-Yue Chen, Tsao-Chi Chuang, Ssu-Yen Huang, Hung-Wei Yen, and Chi-Feng Pai*, “*Spin-orbit torque from a magnetic heterostructure of high-entropy alloy*” Physical Review Applied 8 (4), 044005(2017)
- [13] Tian-Yue Chen, Chun-Te Wu, Hung-Wei Yen, and Chi-Feng Pai*, “*Tunable spin-orbit torque in Cu-Ta binary alloy heterostructures*” Physical Review B 96 (10), 104434 (2017)

摘要

非揮發性自旋軌道矩磁阻式記憶體具有快速、高密度、低耗能之特性，因此被認為是極具有發展潛力的次世代記憶體。而過渡金屬因為具有較強的自旋軌道耦合效應及自旋霍爾效應，所以廣泛的被使用為自旋元件中自旋軌道矩來源材料。為了達成更高密度及更低耗能，自旋軌道矩元件必須具有良好的垂直異向性及更高的自旋軌道矩轉換效率。然而，具有垂直異向性的自旋軌道矩元件，因為必須外加水平磁場破壞對稱性，才能達成電流致磁矩翻轉，導致在應用發展上產生瓶頸。因此，達成零外加場電流致磁矩翻轉，是目前急切需要解決的課題。

在本論文中，首先製備了以過渡金屬為主且具有垂直異向性的自旋軌道矩元件。藉由磁滯曲線偏移法及電流致磁矩翻轉量測，分析了在元件中的自旋軌道矩轉換效率。同時也探討了薄膜介面間的自旋穿透率，元件熱穩定性及磁性材料中的自旋霍爾效應。

接著，利用過渡金屬合金系統來進一步調整自旋軌道矩效率。在以鉻元素為主的二元合金自元件中，發現其自旋軌道矩效率可以藉由控制薄膜的電阻率而改變。而透過電流致翻轉量測，也發現在微米尺寸元件中的磁矩翻轉行為，較適合以自旋軌道矩輔助磁疇擴張的機制描述。除了二元合金外，也製備了五元高熵合金的自旋元件，並探索在複雜合金系統中的自旋霍爾效應。結果證實在隨機混合的合金系統中，有機會能達到更高的自旋軌道矩效率。

最後，研究的重點轉向在具有垂直異向性的自旋軌道矩元件中達成零外加場磁矩翻轉。近年的研究提出，由垂直方向的自旋極化誘發的特殊自旋軌道矩可以導致零磁場磁矩翻轉。這些特殊自旋極化現象，通常可以在具有低對稱性材料中被觀察到。然而，這些材料的製備方式都非常複雜且難以整合在工業製程中。在這個研究中，驗證了此特殊自旋極化可以在由濺鍍系統製備的具刻面磁性結構被觀察到，且能有效地達成零磁場致磁矩翻轉。除此之外，此特殊自旋極化現象，也顯現在單一極性的翻轉行為上。此結果證實具有刻面結構的材料可以成為產生

垂直自旋極化的自旋矩來源材料。

本篇論文針對自旋軌道矩元件中所需要的自旋軌道矩效率、自旋穿透率、熱穩定性、及過渡金屬中的自旋軌道矩進行了完整的討論，並針對調控自旋軌道矩效率及零磁場磁矩翻轉也提供了有效的驗證，也期許能在自旋軌道矩磁阻式記憶體的發展上做出貢獻。

關鍵字：過渡金屬、磁性材料、垂直異向性、自旋霍爾效應、自旋軌道矩、零磁場致磁矩翻轉

ABSTRACT

Nonvolatile spin-orbit torque (SOT) magnetic random access memory (MRAM) is a promising candidate for next-generation memory due to its fast speed, high density, and low power-consumption. Among all metals, transition metals (TMs) are reported to have the sizable spin Hall effect (SHE) with strong spin-orbit coupling (SOC), which is widely served as the SOT source layer in SOT magnetic device. To reach the higher density and the lower energy-consumption, the perpendicular magnetic anisotropy (PMA) and the giant charge-to-spin conversion efficiency are desirable for novel SOT-MRAM unit. However, the necessity of the external field for reaching deterministic SOT switching in PMA SOT device is harmful for further application. Thus, achieving the field-free SOT switching has become a significant issue for PMA SOT-MRAM.

In this dissertation, the PMA SOT devices based on TMs are firstly prepared and the SOT efficiencies are systematically studied through the hysteresis loop shift measurement and the current-induced SOT switching measurement. Along with the SOT analysis, the spin transparency between TM/ferromagnet interface, thermal stability, and the SHE in magnetic materials are consequently discussed by $5d$, $4d$, and $3d$ TMs. To further engineer the DL-SOT efficiency, the Ta-based binary alloy system is employed as the buffer layer. It shows that the DL-SOT efficiency can be linearly tuned by adjusting the buffer layer resistivity. Current-induced SOT switching analysis

further reveals the switching behavior is better explained by a SOT-assisted domain wall propagation picture in micron-size Hall bar device. Further SOT exploration of a quinary high-entropy alloy (HEA) verifies it is possible to reach sizable SOT by working on randomly mixing alloy.

Last, it turns focus on the field-free SOT switching in PMA SOT device. Recently, seminal works suggest that the out-of-plane (OOP) spin polarization induced unconventional SOT in low-symmetry material system is an alternative to realize field-free switching. However, the preparation processes can be complicated and challenging to achieve in industrial fabrication facilities. Here, an all-sputter-prepared magnetic heterostructures with faceted structure demonstrates the SOT switching can be induced by both conventional SOT and unconventional OOP spin polarization. More importantly, the unidirectional field-free switching feature examines the existence of OOP spin polarization. It suggests that materials with strong faceted structures can serve as potential SOT sources with OOP spin polarization.

The dissertation systematically discusses the issues of current SOT technology and provides information to make progress on advanced spintronics memory.

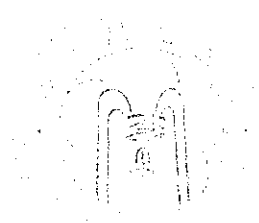
Key words: Transition metal, Magnetic material, Perpendicular magnetic anisotropy, Spin Hall effect, Spin-orbit torque, Field-free SOT switching

TABLE OF CONTENTS

口試委員會審定書	i
致謝.....	ii
LIST OF PUBLICATIONS.....	iv
摘要.....	vi
ABSTRACT.....	viii
TABLE OF CONTENTS.....	x
LIST OF FIGURES	xiv
LIST OF TABLES.....	xxii
Chapter. 1 Introduction.....	1
1.1 Magnetic random access memory.....	1
1.2 Spin-orbit torque and perpendicular magnetic anisotropy.....	2
1.3 Field-free spin-orbit torque switching	3
1.4 Motivation.....	4
Chapter. 2 Theoretical background	5
2.1 Magnetoresistance.....	5
2.1.1 Ordinary magnetoresistance and anisotropy magnetoresistance	6
2.1.2 Giant magnetoresistance	8
2.1.3 Tunnel magnetoresistance.....	9
2.2 Hall effects	11
2.2.1 Ordinary Hall effect	11
2.2.2 Anomalous Hall effect	12
2.2.3 Spin Hall effect	14
2.3 Magnetic anisotropy.....	16
2.4 Magnetization dynamics	20
2.4.1 Landau-Lifshitz-Gilbert equation	20
2.4.2 Dzyaloshinskii-Moriya Interaction	22
2.4.3 Domain wall.....	24
2.5 Spin torque.....	25
2.5.1 Spin-transfer torque	25
2.5.2 Spin-orbit torque	28
Chapter. 3 Fabrication and measurements	33
3.1 Magnetron sputtering.....	34

3.2	Magneto-optical Kerr effect.....	35
3.3	Vibration sample magnetometry	37
3.4	Photolithography.....	39
3.5	Ion milling and secondary ion mass spectrometer	42
3.6	Spin-orbit torque measurements	44
3.6.1	Hysteresis loop shift measurement	45
3.6.2	Current-induced SOT switching	48
Chapter. 4	Spin-orbit torque generation in pure transition metal	51
4.1	Introduction.....	51
4.2	Spin-orbit torque and spin transparency	52
4.2.1	Ta-based magnetic heterostructures	53
4.2.2	W-based magnetic heterostructures	56
4.3	Spin-orbit torque and thermal endurance.....	59
4.3.1	Magnetic properties	60
4.3.2	Hysteresis loop shift measurement	61
4.3.3	Current-induced SOT switching and thermal stability	63
4.4	Spin-orbit torque and spin Hall effect in magnetic materials	66
4.4.1	Spin-orbit torque generation	66
4.4.2	Spin-orbit torque characterization.....	68
4.5	Summary	73
Chapter. 5	Engineering the spin-orbit torque efficiency by alloying	75
5.1	Introduction.....	75
5.2	Tunable spin Hall effect in Ta alloy	76
5.2.1	Electrical measurement and structural properties	77
5.2.2	Spin-orbit torque measurements	80
5.2.3	Resistivity engineering.....	86
5.3	Spin Hall effect in a quinary high-entropy alloy.....	87
5.3.1	Structural properties	89
5.3.2	Spin-orbit torque characterizations	90
5.4	Summary	95
Chapter. 6	Field-free spin-orbit torque switching driven by facet-induced out-of-plane spin polarization.....	97
6.1	Introduction.....	97

6.2	Structural and magnetic properties	99
6.3	Spin-orbit torque characterization.....	101
6.4	Conventional current-induced spin-orbit torque switching	105
6.5	Unconventional field-free spin-orbit torque switching.....	107
6.6	Summary	113
Chapter. 7	Conclusion and future outlook	115
Appendix.....		119
A.	Resistivity estimation.....	119
B.	VSM measurement.....	121
Bibliography		131



LIST OF FIGURES

Figure 2-1. Illustration for the mechanism of anisotropy magnetoresistance. (a) High resistance. (b) Low resistance. (c) Field-scan and (d) angle-scan AMR results from a W(4)/CoFeB(4) /MgO(2)/Ta(2) device with IMA. The angle is between current channel and applied external field.	7
Figure 2-2. Illustration of giant magnetoresistance mechanism. (a) Results from Fe/Cr superlattice. Figure replotted from [48]. (b) Low resistance. (c) High resistance.....	9
Figure 2-3. The magnetic tunnel junction. (a) Illustration of parallel state and anti-parallel state. (b) Field-scan TMR loop. (c) TEM image of a CoFeB/MgO/CoFeB MTJ. Figure reprinted from [55].	10
Figure 2-4. Illustration of ordinary Hall effect.	11
Figure 2-5. Illustration of three main mechanisms contribute to anomalous Hall effect. (a) Intrinsic deflection. (b) Side jump. (c) Screw scattering.....	13
Figure 2-6. (a) Illustration of anomalous Hall effect (AHE). (b) Out-of-plane AH loop from a W(4)/CoFeB(1.4)/MgO(2)/Ta(2) device with PMA.	14
Figure 2-7. (a) Illustration of spin Hall effect (SHE). (b) Side-view of SHE.....	16
Figure 2-8. Out-of-plane hysteresis loops from (a) Ta(6)/CoFeB(1.4)/Hf(0.5)/MgO(2)/Ta(2), (b) W(4)/CoFeB(1.4)/MgO(2)/Ta(2), (c) Mo(4)/CoFeB(1.4)/MgO(2)/Ta(2), and (d) Pt(4)/Co(0.5)/Pt(2). These loops are obtained by anomalous Hall effect measurement.	18
Figure 2-9. Out-of-plane hysteresis loops from (a) Co ₆₃ Tb ₃₇ (6) and (b) Co ₇₃ Gd ₂₇ (12). The out-of-plane coercive field as functions of (c) CoGd thicknesses and (d) Gd contents.....	20
Figure 2-10. The precessional magnetization described by LLG equation.	21

Figure 2-11. Illustration of the Dzyaloshinskii-Moriya interaction between two moments and large spin-orbit torque.....	23
Figure 2-12. Illustration of (a) Bloch wall and (b) Néel wall in a film with PMA. Figure revised from [84].....	24
Figure 2-13. Illustration of spin-transfer torque in ferromagnet (FM1)/non-magnetic material (NM)/ferromagnet (FM2) structure. (b) The spin-transfer torque acting on FM2 makes the moment in FM2 align with FM1 when electron flows from FM1 to FM2.	25
Figure 2-14. Precession of moment (a) without spin-transfer torque and (b) with spin transfer torque.	27
Figure 2-15. Illustration of spin-orbit torque acting on the moment.	29
Figure 2-16. Illustration of current-induced domain wall motion.	30
Figure 2-17. (a) Illustration of a Ta-based three-terminal SOT magnetic device. (b) Current-induced SOT switching result from a Ta-based three-terminal SOT device. Figures revised from [7].	31
Figure 3-1. Illustration of the magnetron sputtering used in the thesis.	35
Figure 3-2. Illustrations of (a) P-MOKE set-up and (b) L-MOKE set-up. (c) Out-of-plane hysteresis loop from a W(4)/CoFeB(1.4)/MgO(2)/Ta(2) thin film. (d) In-plane hysteresis loop from a W(4)/CoFeB(4)/MgO(2)/Ta(2) thin film.	37
Figure 3-3. Illustration of VSM set-up for (a) in-plane direction and (c) out-of-plane direction. (b) In-plane and (d) out-of-plane hysteresis loops from a W(4)/CoFeB(1.6) /MgO(2)/Ta(2) with PMA.	38
Figure 3-4. Process chart of standard photolithography process.	40
Figure 3-5. Process chart of image reversal process.	41
Figure 3-6. Illustrations of(a) single-cross and (b) double-cross Hall bar devices.	42

Figure 3-7. (a) Ion-milling system and SIMS detector. (b) SIMS spectra of a W(5)/CoFeB(4)/MgO(2)/Ta(2) thin film.....	43
Figure 3-8. (a) SIGNAL RECOVERY 7265 lock-in amplifier. (b) Keithley 2400 source meter and (c) Keithley 2000 multimeter44	
Figure 3-9. Illustration of effective field acting on the domain wall (a) without external in-plane field and (b) with external in-plane field.46	
Figure 3-10. (a) The set-up of hysteresis loop shift measurement. (b) Representative hysteresis loop shifts under $H_x = 2500$ Oe and $I_{dc} = \pm 6$ mA from a Pt(4)/Co(1)/ MgO(2) device. The switching fields (H_{sw}) as functions of applied dc currents with (c) $H_x = 2500$ Oe and (d) $H_x = 0$ Oe. Figure is revised from [66].....48	
Figure 3-11. Representative current-induced switching loops from (a) W(4)/CoFeB(1.4) /MgO(2)/Ta(2) PMA device and (b) W(4)/CoFeB(2)/MgO(2)/Ta(2) IMA device. Pulse-width dependence of critical switching current from a (c) W(4)/CoFeB(1.4)/MgO(2) /Ta(2) device and a (d) W(4)/CoFeB(2)/MgO(2) /Ta(2) device.50	
Figure 4-1. (a) Out-of-plane hysteresis loop, (c) effective fields as functions of applied currents, and (e) current-induced SOT switching from a Ta(6)/CoFeB(1.4)/ Hf(0.5)/MgO(2)/Ta(2) device. (b) Out-of-plane hysteresis loop, (d) effective fields as functions of applied currents, and (f) current-induced SOT switching from a Ta(6)/Py(1.4)/Hf(0.5)/MgO(2)/Ta(2) device.55	
Figure 4-2. (a) Out-of-plane hysteresis loop, (c) effective fields as functions of applied currents, and (e) current-induced SOT switching from a W(4)/CoFeB(1.4)/Hf(0.5)/MgO(2)/Ta(2) device. (b) Out-of-plane hysteresis loop, (d) effective fields as functions of applied currents, and (f) current-induced SOT switching from a W(4)/CoTb(6)/Ta(2) device.57	

Figure 4-3. MOKE measurement. (a) Representative out-of-plane hysteresis loop form Mo(4)/CoFeB(1.4)/MgO(2)/Ta(2) thin film. (b) Out-of-plane coercive field of Mo(4)/ CoFeB(1.4)/MgO(2)/Ta(2) samples as a function of annealing temperature T_a61

Figure 4-4. Hysteresis loop shift measurement. (a) Schematic illustration of Hall-bar device. (b) Representative hysteresis loop shifts from a Mo(4)/CoFeB(1.4)/MgO(2)/ Ta(2) device. (c) $H_z^{\text{eff}}/I_{\text{dc}}$ versus applied in-plane field H_x . (d) DL-SOT efficiency ξ_{DL} for Mo(4)/CoFeB(1.4)/MgO(2) samples as a function of annealing temperature T_a63

Figure 4-5. Current-induced SOT switching. (a) Reversible SOT switching under $H_x = \pm 800$ Oe. from a Mo(4)/CoFeB(1.4)/MgO(2)/Ta(2) device. (b) Pulse width dependence of critical switching current under $H_x = 800$ Oe.65

Figure 4-6. Illustrations of (a) anomalous Hall effect, (b) planar Hall effect, and (c) spin Hall effect. (d) Measurement configuration of hysteresis loop shift measurement. The yellow, blue, and pink arrows represent the charge current, magnetization, and spin current, respectively.....68

Figure 4-7. Out-of-plane hysteresis loops from (a) Fe(1), (c) Co(2), and (e) Ni(6) devices. Current-induced effective fields as functions of applied currents of (b) Fe(1), (d) Co(2), and (f) Ni(6) magnetic heterostructures.....70

Figure 4-8. Thickness-dependent SOT efficiency of Ni(t).71

Figure 4-9. Current-induced SOT switching loops from (a) Pt(2)/Co(0.5)/Pt(2) trilayer, (b) Fe(1), (c) Co(2), and (d) Ni(6) magentic heterostructures.72

Figure 5-1. (a) Schematic illustration of layer stacks. The black arrows represent the magnetic moment with PMA. (b) The resistivity of $\text{Cu}_{100-x}\text{Ta}_x$ layer as a function of Ta content (atomic percentage).78

Figure 5-2. Cross-sectional HR-TEM images from (a) Cu₇₀Ta₃₀-based (Cu-rich) and (b) Cu₁₀Ta₉₀-based (Ta-rich) magnetic heterostructures. The subpanels show the diffractograms computed by reduced fast Fourier transformation from the regions of interest. Out-of-plane hysteresis loops of (c) Cu₇₀Ta₃₀-based (Cu-rich) and (d) Cu₁₀Ta₉₀-based (Ta-rich) magnetic heterostructures.....80

Figure 5-3. Current-induced SOT switching (a) Hall-bar device illustration (b) A representative current-induced SOT switching curve of a Cu₆Ta₉₄(4)/W(0.5)/CoFeB(1.4)/Hf(0.5)/MgO(2) Hall-bar device under $H_x = 100$ Oe. (c) Representative hysteresis loop shifts from a Cu₁₆Ta₈₄-based device. (d) Summary of effective field with applied current.82

Figure 5-4. Hysteresis loop shift measurement. (a) Representative hysteresis loop shifts from a Cu₁₆Ta₈₄-based device. (b) Summary of effective field with applied current. (c) Out-of-plane coercive filed H_c as a function of Ta content. (d) The measured and estimated critical switching currents as a function of Ta content.....84

Figure 5-5. (a) Resistivity of TaN_x with N₂ flow rate. (b) A summary of DL-SOT efficiency as a function of buffer layer resistivity for both alloying (Cu-Ta) and nitridation (TaN) samples.....87

Figure 5-6. (a) Cross-sectional high-resolution TEM (HRTEM) image of a 57 nm Ta-Nb-Hf-Zr-Ti high entropy alloy (HEA) thin film prepared by magnetron sputtering. (b) Energy-dispersive spectroscopy (EDS) results of the sputtered deposited Ta-Nb-Hf-Zr-Ti HEA film.....89

Figure 5-7. Hysteresis loop shift measurement. (a) Representative hysteresis loop shifts of the $t_{\text{HEA}} = 5$ nm HEA sample under $I_{dc} = 1.1$ mA and $I_{dc} = -0.9$ mA with in-plane bias field $H_x = 500$ Oe. (b) Summary of effective field with applied current. (c) Current-induced field per current density χ as a function of in-

plane field. (d) Thickness-dependent DL-SOT efficiency with HEA-based and Ta-based magnetic devices.....	93
Figure 5-8. Current-induced SOT switching from HEA-based magnetic device under (a) $H_x = 100$ Oe and (b) $H_x = -100$ Oe.....	94
Figure 6-1. (a) Cross-sectional TEM image and (b) XRD diffraction pattern of a sputter-deposited Py(5)/Pt(2)/Co(0.5)/Pt(2) thin film.....	100
Figure 6-2. VSM measurement on Py(5)/Pt(2)/Co(0.5)/Pt(2). (a) IP and OOP M-H loops. (b) M-H loops from positive and negative pre-magnetization field.....	101
Figure 6-3. Hysteresis loop shift measurements on Py(t)/Pt(2)/Co(0.5)/Pt(2) devices. (a) Illustration of a Hall-bar device for electrical measurement. (b) Representative AH loop of a Py(5)/Pt(2)/Co(0.5)/Pt(2) device. (c) Representative shifted hysteresis loops of a Py(5)/Pt(2)/Co(0.5)/Pt(2) device under $I_{dc} = 1.6$ and -1.9 mA. (d) H_z^{eff} as functions of I_{dc} under $H_x = \pm 500$ Oe and $H_x = 0$ Oe. (e) H_z^{eff}/I_{dc} as a function of H_x for a Py(5)/Pt(2)/Co(0.5)/Pt(2) device. (f) Py thickness dependence of DL-SOT efficiency. The dashed line represents the fitting to a spin diffusion model.....	103
Figure 6-4. DL-SOT efficiency as a function of Py thickness.....	105
Figure 6-5. Conventional current-induced SOT switching. (a) Representative current-induced SOT switching from a Py(5)/Pt(2)/Co(0.5)/Pt(2) device under $H_x = \pm 100$ Oe. (b) Current pulse-width t_{pulse} dependence of critical switching current density J_c under $H_x = 100$ Oe. The lines represent the linear fitting to the experimental data.....	107
Figure 6-6. Unidirectional field-free SOT switching. The illustrations of the field-free SOT switching for (a) $+J_{\text{pulse}}$ and (b) $-J_{\text{pulse}}$ after applying $+H_{\text{sat}}$. (c)	

Representative field-free SOT switching after applying $+H_{\text{sat}}$. The illustrations of the field-free SOT switching for (d) $+J_{\text{pulse}}$ and (e) $-J_{\text{pulse}}$ after applying $-H_{\text{sat}}$. (f) Representative field-free SOT switching after applying $-H_{\text{sat}}$ in a Py(5)/Pt(2)/Co(0.5)/Pt(2) device. The gray arrow represents the initial magnetization state of IP magnetized Py. The red (blue) arrow stands for the electron with up (down)-OOP spin polarization. Currents flow along high symmetry axis with initial magnetization state of (g) $+m_{\text{Co}}$ and (h) $-m_{\text{Co}}$. (i) Results of SOT switching when currents flowing high symmetry axis with $+m_{\text{Co}}$ and $-m_{\text{Co}}$109

Figure 6-7. Hysteresis loop shift results when currents flowing along high symmetry axis. (a) Representative hysteresis loop shifts under $I_{\text{dc}} = \pm 2.5$ mA. (b) H_{sw} versus I_{dc} in the absence of in-plane external field.110

Figure 6-8. H_x dependence of SOT switching and illustration of SOT effective fields acting on a magnetic domain with Néel type domain walls. (a) SOT switching under $H_x = 5, 0, -3$, and -5 Oe. (b) Critical switching current densities as functions of H_x . (c) When $H_x > 0$, H_{DL} assists with H_{OOP} . (d) For $H_x = 0$, H_{DL} vanishes and H_{OOP} dominates the SOT switching. (e) For $H_x = -3$ Oe, H_{DL} compensates with H_{OOP} . (f) For, $H_x < -3$ Oe, H_{DL} partially cancels by H_{OOP} and the total effective field is negative ($H_z^{\text{eff}} < 0$). Gray and orange arrows represent the domain wall moments and PMA Co magnetization. White and yellow arrows stand for the y - and z -direction spin polarization, respectively. Red and blue arrows indicate the effective field (H_{DL}) generated from IP DL-SOT. Light green arrow is the OOP spin polarization induced OOP effective field (H_{OOP}).....112

Figure B- 1. (a) VSM wafer size illustration. In-plane and out-of-plane M-H loops from
(b) Ta/Co₂₀Fe₆₀B₂₀/Hf/MgO, (c) HEA/Co₂₀Fe₆₀B₂₀/Hf/MgO, (d) W/
Co₄₀Fe₄₀B₂₀/MgO, (e) Mo/Co₄₀Fe₄₀B₂₀/ MgO, (f) Ta/Py/Hf/MgO, (g) Pt/
Co/Pt, and (h) W/CoTb/Ta.....123

Figure B- 2. Saturation magnetization and magnetic dead layer of (a) Ta/CoFeB/Hf/
MgO, (b) HEA/CoFeB/Hf/MgO, (c) W/CoFeB/MgO, and (d) Mo/CoFeB/
MgO.....124

Figure B-3. Saturation magnetization (M_s) and magnetic dead layer (t_{dead}) of (a) Ta/Py/
Hf/MgO, (b) Pt/Co/Pt, and (c) W/CoTb/Ta.....125

Figure B-4. Effective anisotropy of (a) Ta/CoFeB/Hf/MgO, (b) HEA/CoFeB/Hf/MgO,
(c) W/CoFeB/MgO, and (d) Mo/CoFeB/MgO.....127

Figure B-5. Effective anisotropy of (a) Ta/Py/Hf/MgO, (b) Pt/Co/Pt, and (c) W/CoTb/
Ta.....128

LIST OF TABLES

Table 4-1. Summary of DL-SOT efficiency (ξ_{DL}) and critical switching current density (J_c).....	58
---	----

Table B- 1. Summary of saturation magnetization (M_s), magnetic dead layer (t_{dead}), interfacial anisotropy energy (K_s), and volume anisotropy energy (K_v). 129

